The Alcock Paczynski test with voids in 21 cm intensity field

Takao Endo,[1] Hiroyuki Tashiro[1] and Atsushi J. Nishizawa [1,2]⋆

[1]*Graduate School of Science, Nagoya University, Aichi 464-8602, Japan*
[2]*Institute for Advanced Research, Nagoya University, Aichi 464-8602, Japan*

ABSTRACT

Feasibility of the Alcock Paczynski (AP) test by stacking voids in the 21 cm line intensity field is presented. We analyse the IllustrisTNG simulation to obtain the 21 cm signal map. We then randomly distribute particles depending on the 21 cm intensity field to find voids by using publicly available code, VIDE. As in the galaxy clustering, the shape of the stacked void in the 21 cm field is squashed along the line of sight due to the peculiar velocities in redshift space, although it becomes spherical in real space. The redshift-space distortion for the stacked void weakly depends on redshift and we show that the dependency can be well described by the linear prediction, with the amplitude of the offset being free parameters. We find that the AP test using the stacked voids in a 21 cm intensity map is feasible and the parameter estimation on Ω_m and w is unbiased.

Key words: cosmological parameters – large-scale structure of Universe – cosmology: theory.

1 INTRODUCTION

Recent developments in observations drive the remarkable progress in cosmology. Based on the fruitful observational data, we can obtain the precise constraint on the theoretical scenarios and models of the Universe. On the other hand, these observations throw up new challenges to us for understanding the Universe. One of them is the discovery of the accelerating expansion of the Universe (Riess et al. 1998; Perlmutter et al. 1999) The most accepted hypothesis to explain this acceleration is dark energy. Dark energy has large negative pressure and can generate a repulsive gravitational force to accelerate the cosmic expansion (Weinberg et al. 2013). The joint analysis among the cosmic microwave background (CMB) anisotropy measurement and galaxy surveys favour the existence of dark energy (Planck Collaboration VI 2020). However, there are not sufficient observations to determine its nature precisely. Therefore it is required to make further efforts to perform CMB anisotropy observations and galaxy surveys more precisely and conduct cosmological observations independent of them.

The Alcock Paczynski (AP) test (Alcock & Paczynski 1979) is also one of the independent observations to probe the expansion history of the Universe. For the success of the AP test, it is required to know physical size of observation objects along the line of sight and angular direction, or the ratio between them. Therefore, the objects whose shapes are spherical or isotropic are the ideal targets for the AP test. There are many works to study the AP test with cosmological objects. The peak scale of the Baryon Acoustic Oscillation (Hu & Sugiyama 1996; Eisenstein et al. 2005) might be one of the best candidates for the AP test because the peak scale is isotropic and well determined by the linear theory and observations (Komatsu et al. 2011; Planck Collaboration VI 2020). Since objects whose shapes are statistically isotropic are also preferable for the AP test, the correlation function

of galaxies and the matter power spectrum are studied as objects for the AP test (Ballinger, Peacock & Heavens 1996; Matsubara & Suto 1996; Hu & Haiman 2003; Seo & Eisenstein 2003; Matsubara 2004; Glazebrook & Blake 2005)

Now cosmic voids have been paid attention as cosmological structures to probe the Universe. While some authors investigated the relation of void size distribution to the cosmological models (Clampitt, Cai & Li 2013; Pisani et al. 2015; Zivick & Sutter 2016; Endo, Nishizawa & Ichiki 2018; Verza et al. 2019). the application of voids also has been studied. The AP test with voids was originally proposed by Ryden (1995). Ryden (1995) demonstrated the AP test with voids in the toy model where individual shapes of voids are assumed to be spherical. However, matter density simulations suggest that their real shapes are far from spherical (van de Weygaert & van Kampen 1993; Shandarin, Sheth & Sahni 2004; Shandarin et al. 2006; Park & Lee 2007; Platen, van de Weygaert & Jones 2008). From the observation side, Sutter et al. (2012b), Sutter et al. (2014a) showed that actual voids are not spherical through applying the watershed algorithm to measure void shapes in observed data. To solve this shape problem in the AP test, Lavaux & Wandelt (2012) have proposed to use the statistical shapes of voids in the AP test. They have argued that the stacked voids can be applied to the AP test because they are expected to be spherical based on the cosmological principle, the statistical isotropy of the Universe.

Up to the present, there have been several studies on this topic. Sutter et al. (2012a) first applied the stacking method to the AP test for the constraint on the matter-energy density parameter Ω_m with voids detected by the galaxy survey, the Sloan Digital Sky Survey (SDSS) Data Release 7 (Abazajian et al. 2009). However, their AP test could not provide the constraint on Ω_m because of the insufficient number of observed voids at that time. Later, (Sutter et al. 2014b) and Mao et al. (2017) revisited the AP test with stacked voids detected from SDSS Data Release 10 (Ahn et al. 2014) and 12 (Alam et al. 2015). Although they have obtained the constraint on Ω_m, the constraints are weak compared with those from other

⋆ E-mail: atsushi.nishizawa@iar.nagoya-u.ac.jp

cosmological observations. One of the challenges in the AP test with voids is modelling of the redshift-space distortions (RSDs). They introduce the anisotropic distortion in the shapes of voids in the redshift space. Without appropriate modelling of the RSDs, the AP test cannot provide the better cosmological constraints. Recently, Hamaus et al. (2015, 2016) addressed the RSD effects on the AP tests of galaxy voids. Their RSD models allowed us to obtain a 10 per cent measurement of Ω_m from the BOSS CMASS sample. More recently, Correa et al. (2019) reach similar conclusions in the galaxy void AP test based on a simulation study.

The precision and tightness of the constraint by the AP test depend on the statistical spherical symmetry of void shapes in an observation data set. To recover the spherical symmetry, a large number of void samples are required. For this reason, we need a huge survey volume, covering a wide range of the sky and reaching deep redshift. The future 21 cm intensity mapping survey by the Square Kilometre Array (SKA) is planned to investigate the huge volume overwhelming the conventional galaxy surveys (Santos et al. 2015; Square Kilometre Array Cosmology Science Working Group et al. 2020). In the previous works, voids are found in the distribution maps of galaxies produced by galaxy surveys. On the other hand, SKA traces the distribution of neutral hydrogen H_I in large-scale structure by measuring the 21 cm line signals caused by their hyperfine structure transition. The void regions also could be observed as low-intensity regions in the 21 cm intensity maps. If we detect the voids from the H_I intensity fields, we will obtain the number of voids more than the galaxy survey.

In this paper, we propose the AP test with void regions in the 21 cm intensity map. We use the contour of the intensity to find out voids in the 21 cm intensity map. When we plot the contour for the appropriate intensity, we can find that the sizable low-density regions are enclosed by the contour. Similar to voids in the galaxy survey map, we can assume that voids in the 21 cm intensity map are statistically spherical according to the cosmological principle. Using the state-of-the-art cosmological hydrodynamics simulation data, we conduct the void findings by the contour in the 21 cm intensity map and show that our assumption about the statistical spherical symmetry is valid. We also perform the AP test with stacking the found voids and demonstrate that the AP test of the stacked voids in the intensity maps can provide the tight constraint with the survey volume planned in the SKA project.

2 METHOD

The aim of this paper is to demonstrate the feasibility of the AP test using the contour lines on the 21 cm intensity map. In this section, we present how we construct the 21 cm intensity map from numerical simulation data.

2.1 Hydrodynamical simulation

The 21 cm signal depends on the number density and temperature of the intergalactic medium (IGM) gas. Therefore, to predict the cosmological 21 cm intensity map properly, the cosmological hydrodynamics simulation is required. In this paper, we used the data of the state-of-the-art cosmological magnetohydrodynamical simulation, called IllustrisTNG (Marinacci et al. 2018; Naiman et al. 2018; Nelson et al. 2018, 2019; Pillepich et al. 2018; Springel et al. 2018). The simulation solves the gravitational force by a Tree-PM scheme (Xu 1995) and hydrodynamics by running a moving-mesh code, the AREPO code (Springel 2010). The simulation also includes a wide range of astrophysical processes, which provide large impacts

on the gas state in the IGM, such as radiative cooling, star formation, stellar evolutions, stellar feedback, growth of supermassive black holes and their feedbacks, and magnetic fields (Nelson et al. 2019). Among the series of the Illustris simulation results, we adopt the IllustrisTNG300-3 data. The size of simulation box is 205 Mpc h^{-1} (in comoving units) on a side and the dynamics of 2×625^3 dark matter particles and gas cells were solved simultaneously.

Using this data, we construct the 21 cm intensity maps. The 21 cm intensity depends on the physical state of the IGM gas. To evaluate the 21 cm signal simply, we prepare a 256^3 grid space in the simulation box and calculate the physical gas quantities in each cell with the Cloud-in-Cell scheme. The simulation treats the gas component as a finite size cell but the size of the cell is enough smaller than the grid separation. Therefore, we can consider the gas as a particle and neglect the finite size effect of the gas. In the simulation, the cosmological parameters are based on the Planck 2015 measurements (Planck Collaboration XIII 2016): $\Omega_m = 0.3089$, $\Omega_\Lambda = 0.6911$, $\Omega_b = 0.0486$, $\sigma_8 = 0.8159$, $n_s = 0.9667$ and $H_0 = 100h \, \mathrm{km \, s^{-1} \, Mpc^{-1}}$ with $h = 0.6774$.

2.2 H_I intensity map

2.2.1 The differential brightness temperature

Neutral hydrogen atom emits or absorbs specific electromagnetic radiation whose wavelength corresponds to 21 cm when its spin configuration between proton and electron, i.e. hyperfine structure, changes. When we observe the cosmological 21 cm signal, we measure it as a difference from the CMB brightness temperature (Furlanetto, Oh & Briggs 2006),

$$\delta T_b = \frac{[T_s(z) - T_{CMB}(z)] \left(1 - e^{-\tau_{10}}\right)}{1 + z}, \tag{1}$$

where δT_b, T_{CMB}, and T_s are the differential brightness temperature, the CMB temperature, and the spin temperature which is defined as the population ratio between the upper and lower states of the hyperfine structure in neutral hydrogen, respectively. The optical depth τ_{10} for the 21 cm line is

$$\tau_{10} = \int ds \, \frac{3}{32\pi} \frac{h_p c^2 A_{10}}{\nu_* k_B} \frac{n_{H_I}}{T_s} \phi(\nu), \tag{2}$$

where h_p is the Planck constant, c is the speed of light, the subscript 10 represents the value corresponding to the energy gap between hyperfine structure levels, $\nu_* = 1.4$ GHz, $A_{10} = 2.85 \times 10^{-15} \, \mathrm{s^{-1}}$ is the Einstein A coefficient of the transition, k_B is the Boltzmann constant, and n_{H_I} is the number density of neutral hydrogen. In equation (2), $\phi(\nu)$ is a line profile which has a peak at the frequency ν_* and satisfies the normalization, $\int \phi(\nu) d\nu = 1$. The line profile suffers the broadening due to the velocity of the H_I gas in the line-of-sight direction, $V_{\parallel}$, which includes the velocities due to the Hubble expansion, the peculiar velocity and the thermal velocity of the gas. Accordingly, the width of the profile is broadened and the amplitude is suppressed by $c/\nu_* V_{\parallel}$ around the peak frequency. Performing the integration in equation (2) with this broadening, we obtain

$$\delta T_b = \frac{3c^3}{32\pi} \frac{A_{10} h_p n_{H_I}}{k_B \nu_*^2} \frac{1}{(1+z)^2 |dV_{\parallel}/dx_{\parallel}|} \left(1 - \frac{T_{CMB}(z)}{T_s(z)}\right), \tag{3}$$

where $dV_{\parallel}/dx_{\parallel}$ is the gas velocity gradient along the line of sight. In the redshifts and scales that we are interested in throughout this paper, we assume that the dominant contribution to $V_{\parallel}$ comes from the Hubble expansion (Horii et al. 2017). Thus, we can approximate
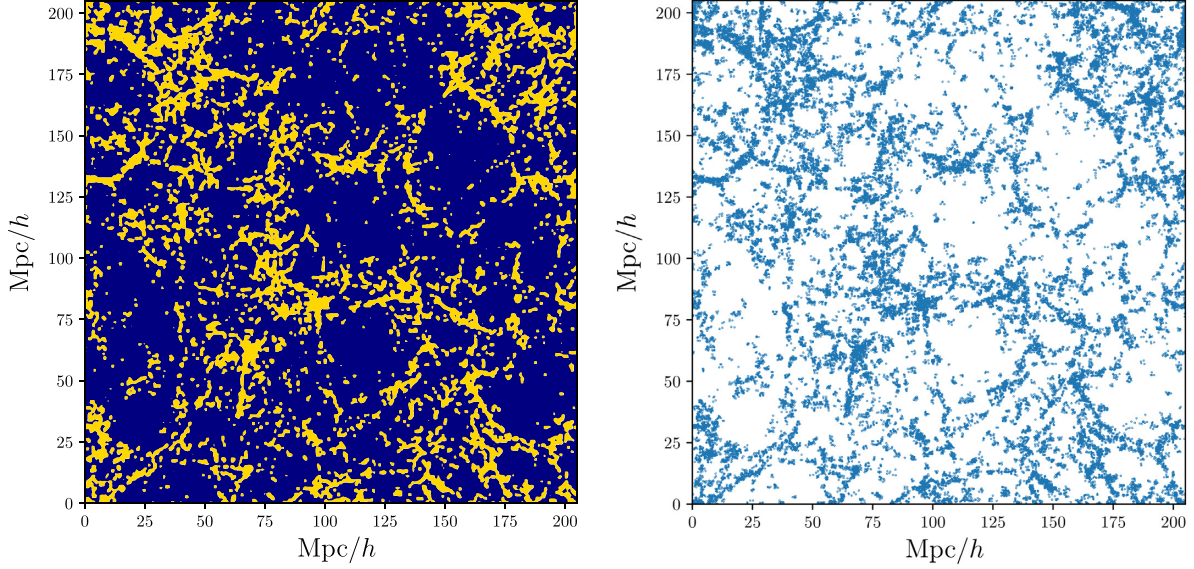
Figure 1. The intensity contour map made from the IllustrisTNG simulation (left-hand panel) and the mock H$_I$ particle distribution (right-hand panel) made from the left-hand panel by means of the method described in Section 2.3. The contour level of the left-hand panel is average brightness temperature $\langle \delta T_b \rangle$ so that we can regard as the dark regions as voids while bright regions as filaments or haloes. In the right-hand panel, we can see that the distribution of mock particles traces the shape of void regions in the left-hand panel.

the velocity gradient as

$$\frac{dV_\parallel}{dx_\parallel} \approx \frac{H(z)}{(1+z)}. \tag{4}$$

2.2.2 Spin temperature

The spin temperature is determined by the balance related to the spin flipping physics in the hyperfine structure including the coupling with CMB photons, thermal collisions with electron and other atoms, and the pumping by the background Ly α photons, which is known as the Wouthuysen–Field effect (Wouthuysen 1952; Field 1958). As a result, the spin temperature can be expressed as (Field 1959; Furlanetto et al. 2006)

$$T_s^{-1} = \frac{T_{\rm CMB}^{-1} + x_c T_K^{-1} + x_\alpha T_\alpha^{-1}}{1 + x_c + x_\alpha}, \tag{5}$$

where T_K and T_α are the kinetic temperature of H$_I$ gas and the colour-temperature of the Ly α radiation field. Throughout this work, we assume $T_\alpha \simeq T_K$. In the equation, x_c and x_α are the coupling coefficients for the thermal collisions and the Ly α photons, respectively. The coupling coefficient x_c is described by

$$x_c = \frac{T_*}{A_{10} T_{\rm CMB}} (n_{\rm H_I} \kappa_{\rm H_I} + n_p \kappa_p + n_e \kappa_e), \tag{6}$$

where $T_* = h_p \nu_* / k_B = 0.068$ K, and n_p and n_e are the number densities of protons and electrons respectively. We need collision rates $\kappa_{\rm H_I}$, κ_p, and κ_e to calculate x_α. We follow the same manner in Kuhlen, Madau & Montgomery (2006) which uses fitting formulae based on Field (1958), Smith (1966), Allison & Dalgarno (1969), Liszt (2001), and Zygelman (2005). In the unit of (cm^3 s^{-1}), these coefficients are given in

$$\kappa_{\rm H_I} = 3.1 \times 10^{-11} T_K^{0.357} \exp\left(\frac{-32}{T_K}\right), \tag{7}$$

$$\kappa_e = \begin{cases} 10^{-9.607+0.5\log(T_K)\exp(-(\log T_K)^{4.5}/1800)} & (T_K \leq 10^4), \\ \kappa_e(T_K = 10^4) & (T_K > 10^4), \end{cases} \tag{8}$$

$$\kappa_p = 3.2\kappa_H, \tag{9}$$

where T_K is in the unit of (K).

The coupling coefficient x_α can be approximated as (Furlanetto et al. 2006)

$$x_\alpha = S_\alpha \frac{J_\alpha}{J_\nu^c}, \tag{10}$$

where $J_\nu^c = 1.165 \times 10^{-10}[(1+z)/20]$ cm^2 s^{-1} Hz^{-1} sr^{-1}, and J_α is the background Ly α photon intensity. The scattering amplitude factor, S_α, is approximated as

$$S_\alpha \sim \exp\left[-0.803 T_K^{-2/3}\left(\frac{10^{-6}}{\gamma}\right)^{1/3}\right], \tag{11}$$

where

$$\gamma = \frac{H(z)\nu_\alpha}{\chi_\alpha n_{\rm H_I} c}, \tag{12}$$

with the Ly α frequency $\nu_\alpha = 2.47 \times 10^{15}$ Hz and

$$\chi_\alpha = \frac{\pi e^2}{m_e c} f_\alpha, \tag{13}$$

where e is the electron charge, m_e is the electron mass, and $f_\alpha = 0.4162$ is the oscillator length. For J_α, we adopt the results in Haardt & Madau (2012).

2.2.3 Intensity contour map from the Illustris data

Following Sections 2.2.1 and 2.2.2, we obtain the 21 cm intensity (the differential brightness temperature) maps from the IllustrisTNG300-3 simulation data. In the left-hand panel of Fig. 1, we show the
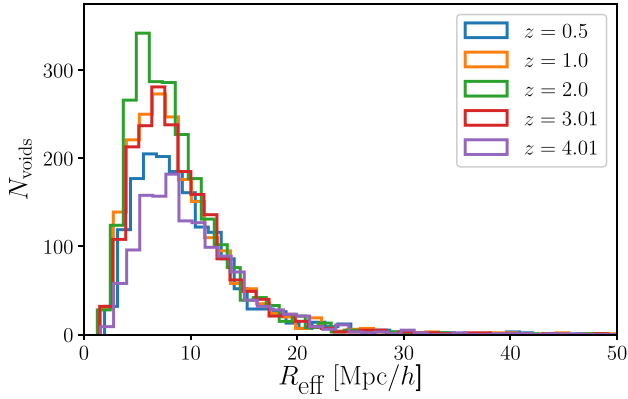
Figure 2. The size distribution of the voids at different redshifts. In our simulation, voids are populated mainly at $5\,\mathrm{Mpc}\,h^{-1} < R_{\mathrm{eff}} < 10\,\mathrm{Mpc}\,h^{-1}$ and increase till $z = 2$ and decrease afterwards.

contour map of the intensity at $z = 1$. Here we take one contour line corresponding to the averaged intensity $\langle \delta\,T_{\mathrm{b}} \rangle$ in the simulation box to make the contour map. The bright colour regions have larger intensity than the average value, while the dark colour regions have lower intensity. Since the intensity is proportional to the $H\,\text{I}$ density, the dark regions can be identified as voids.

Each dark region surrounded by the bright filamentary structures is not spherical. However, the cosmological principle allows us to make a hypothesis that the dark regions are statistically spherical and to apply the stacked shape of the low-intensity regions to the AP test. To extract each shape of the dark region as a void in the contour map, we adopt publicly available code VIDE (Sutter et al. 2015). In the next subsection, we describe how we apply the void finding to our contour maps.

2.3 Void finding

To trace the shape of the dark (low-intensity) regions in the left-hand panels of Fig. 1, we exploit the VIDE algorithm (Sutter et al. 2015). This algorithm is an updated version of the ZOBOV algorithm (Neyrinck 2008) which uses the Voronoi tessellation to make a density field and applies the watershed method (Platen, van de Weygaert & Jones 2007) to detect void regions.

The VIDE algorithm finds out voids based on a particle distribution. Therefore, we need to construct the particle distribution from the 21 cm intensity contour map as shown in Fig. 1. Since the dark regions are encircled by the bright regions, we put a particle in each grid of the bright regions. In the right-hand panel of Fig. 1, we show the mock particle distribution obtained from the left-hand panel. One can see that the mock particle distribution traces the outlines of the dark regions on the left-hand panel.

Now we can obtain the statistical property of the dark regions as 'voids' using the VIDE algorithm with the mock particle distribution. We show the obtained void abundance in Fig. 2 where the x-axis represents the effective comoving radius of a void as

$$R_{\mathrm{eff}} = \left(\frac{3}{4\pi}V\right)^{1/3}, \tag{14}$$

where V is the volume of the void region evaluated by the VIDE algorithm. To represent the redshift dependence, we also provide the void abundance at different redshifts, $z = 0.5,\ 1,\ 2,\ 3,$ and 4 by using the snapshot data at those redshifts.

The abundances of voids in our catalogues have peaks between $R_{\mathrm{eff}} = 5$ and $10\,\mathrm{Mpc}\,h^{-1}$. Until $z = 2$, the void abundance increases overall scales of voids, since the structure formation evolves as the redshift decreases. However, after $z = 2$, the merger among small voids is important in the void evolution. While the merger events decrease the number of small voids, they enhance the abundance of large voids. We note that the threshold is a free parameter in our methods although we set the threshold to the average intensity to create the mock particle distribution. When we increase the threshold, the total number of voids decreases. On the other hand, when we decrease the threshold, the abundance of voids, in particular, small-scale voids, increases because the VIDE algorithm identifies the substructure in large voids due to the low threshold.

We note that in real observation, we find voids in observational space, i.e. frequency ν as a line of sight and angles θ as a perpendicular plane to the line of sight. Then the ratio of the sizes in ν to θ direction can be compared by assuming various cosmological models. In our analysis, since we do not have the void finding tool working on the observation (ν, θ) space, instead, we find voids in Cartesian coordinates directly using the simulation. Then assuming a *true* underlying cosmological parameters, we convert it to the observation plane. Therefore, the void catalogue obtained in such a way corresponds to the one we will obtain when we have an ideal observation in terms of spatial and frequency resolutions and if we have the tool to find voids in observation space without any additional systematic uncertainties.

3 THE AP TEST WITH STACKED VOIDS

3.1 The AP test

The AP test can determine the cosmological model by using the known geometrical information about the target objects (Alcock & Paczynski 1979). Suppose that we observe an object which has the comoving sizes $\Delta x_{\parallel}$ in the line-of-sight direction and $\Delta x_{\perp}$ in the perpendicular direction. If it is located at a cosmological distance from us, the redshift span Δz of the object corresponding to $\Delta x_{\parallel}$ is

$$\Delta x_{\parallel} = \int_z^{z+\Delta z} \frac{c\,\mathrm{d}z'}{H(z')} \approx \frac{c}{H(z)}\Delta z, \tag{15}$$

where $H(z)$ is the Hubble parameter,

$$H(z) = H_0 \sqrt{\Omega_{\mathrm{m},0}(1+z)^3 + (1-\Omega_{\mathrm{m}})(1+z)^{3(1+w)}}, \tag{16}$$

with the present energy density parameters of matter and the equation-of-state parameter of dark energy, Ω_{m} and w, respectively. Here we have assumed a flat universe. We note that since we will work in the redshifts, $z \leq 4$, we can drop the contribution from the radiation components to the Hubble parameter.

The observed angular scale $\Delta\theta$ of the object is given by

$$\Delta x_{\perp} = \chi(z)\Delta\theta, \tag{17}$$

where $\chi(z)$ is the comoving distance from the observer to the object at the redshift z,

$$\chi(z) = \int_0^z \frac{c\,\mathrm{d}z'}{H(z')}. \tag{18}$$

If the object is spherically symmetric, $\Delta x_{\parallel} = \Delta x_{\perp}$, the observed redshift span and angular size can be related as

$$\frac{\Delta z}{z\Delta\theta} = \frac{1}{cz}\chi(z)H(z). \tag{19}$$

Here, the left-hand side is the observable, while the right-hand side can be calculated from the cosmological model. Therefore, when
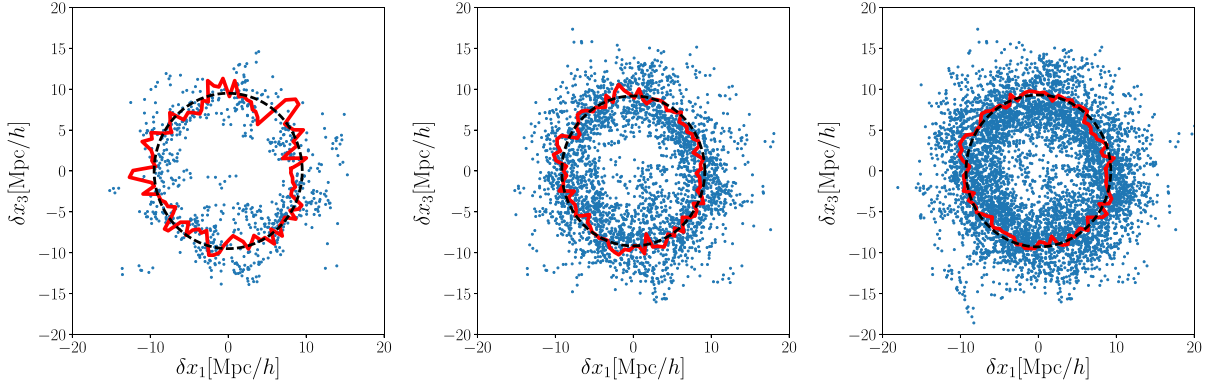
Figure 3. We show how the stacking of void works in real space. From the left-hand panel to the right-hand panel, we stack 10, 50, and 100 voids. We show the two-dimensional stacked voids with $R_{\rm eff} = 10 \pm 0.5\,[\,{\rm Mpc}\,h^{-1}]$ at $z = 1$. The dashed black line shows a reference circle and the solid red line shows averaged particle position within an azimuthal bin. The averaged profile becomes closer to the spherical shape when the number of voids is larger.

the observable and the theoretical prediction from the cosmological model satisfy the relation given in equation (19), the cosmological model used in the prediction is correct to describe our Universe.

3.2 Void stacking

According to the cosmological principle, we can make the hypothesis that the voids found in the 21 cm intensity map as described in the previous section are also statistically spherical symmetric. To check the hypothesis, we stack voids found in the 21 cm map and evaluate the size ratio between $\Delta x_\parallel$ and $\Delta x_\perp$ of the stacked void. In the stacking process, we convert the particle positions in the simulation box into the relative position from the centre of the void,

$$\delta \boldsymbol{x}_i = \boldsymbol{x}_i - \boldsymbol{x}_c. \tag{20}$$

where $\boldsymbol{x}_i$ and $\boldsymbol{x}_c$ are the positions of the ith particle and the centre of the void to which the ith particle belongs. The position of the centre of a void is determined as the Voronoi cell volume-weighted centre,

$$\boldsymbol{x}_c = \frac{\sum V_i \boldsymbol{x}_i}{\sum V_j}, \tag{21}$$

where V_i represents the Voronoi cell volume of the ith particle.

Then, we take the second moment of the stacked particle distribution to determine the size of the stacked void. We assume that the observed voids are enough far from the observer so that we can take the space coordinate systems in which the x_3 axis is the line-of-sight direction, and x_1 and x_2 are the perpendicular direction. In this configuration, the second moments for each direction are evaluated as

$$\Delta x_\parallel^2 = \langle \delta x_3^2 \rangle = \frac{1}{N} \sum_i^N \delta x_{i,3}^2, \tag{22}$$

$$\Delta x_\perp^2 = \frac{\langle \delta x_1^2 \rangle + \langle \delta x_2^2 \rangle}{2} = \frac{1}{N} \sum_i^N \frac{\left(\delta x_{i,1}^2 + \delta x_{i,2}^2 \right)}{2}, \tag{23}$$

where N is the total number of particles to be stacked. We stack voids only within the narrow radial size of $\Delta R_{\rm eff} = 1\,{\rm Mpc}\,h^{-1}$, where $5\,{\rm Mpc}\,h^{-1} \le R_{\rm eff} \le 15\,{\rm Mpc}\,h^{-1}$. The information of different size voids is merged in the level of the likelihood as discussed in Section 3.3.

We first visualize the shape convergence according to the number of voids in the two-dimensional stacking in Fig. 3. Here we show the stacked void of the radius $R_{\rm eff} = 10\,{\rm Mpc}\,h^{-1}$ at $z = 1$. We increase
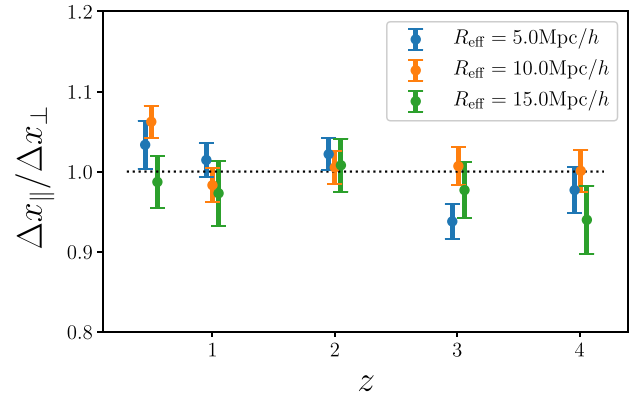

Figure 4. The ratio between $\Delta x_\parallel$ and $\Delta x_\perp$ of the stacked voids in the 21 cm map in real space. The error bar is measured from the one realization of the simulation box. One can see that the size ratio is consistent with unity, which suggests that the shape of the stacked void is spherical in real space. We also see that this property does not depend on the redshift and the size of the stacked void.

the number of voids for stacking as 10, 50, and 100 from the left-hand panel to the right-hand panel respectively. The red solid lines show the averaged particle positions in each sector while the black dotted lines indicate the reference circles. One can see that the shape of the stacked void is noisy when the number of voids is small. On the other hand, the averaged void shape is likely to be spherical when the number of voids is large.

Then, we plot the ratio between $\Delta x_\parallel$ and $\Delta x_\perp$ in Fig. 4. In Fig. 4, we represent the results of the stacked voids of radii $R_{\rm eff} = 5$, 10, and $15\,{\rm Mpc}\,h^{-1}$. To evaluate the error bars, we measure the variance by 100 times bootstrapping, which was sufficient to converge.

The results show us that the statistical error depends on the number of voids. Therefore, the error bar becomes large as the number of voids decreases as shown in Fig. 2. However, the ratio does not deviate from unity more than a 2σ confidence level. This fact strongly supports our hypothesis that the void shape in the contour maps is statistically spherical. Therefore, the voids in the 21 cm contour maps are appropriate for the AP test.

We note that the future SKA intensity mapping survey such as SKA1-MID will cover $20\,000\,{\rm deg}^2$ in the sky (Square Kilometre Array Cosmology Science Working Group et al. 2020). This sky

coverage corresponds to 20 times larger than the simulation size at $z = 0.5$. For higher redshifts, the comoving volume also becomes larger. Thus the statistical error may be roughly reduced by at least $1/\sqrt{20}$ times for the future survey. Therefore, in future surveys, the actual statistical uncertainty for the shape ratio could be smaller than our estimation in Fig. 4.

3.3 Parameter estimation

Let us demonstrate the AP test of the stacked voids in the 21 cm contour maps to determine the cosmological parameter. Here we adopt the Markov Chain Monte Carlo method which is a powerful tool to estimate the parameter from a set of observation signals. This method provides us with the posterior probability of a model parameter based on the Bayes' theorem when we obtain a data set by observations. Suppose we conduct an observation and obtain the observation data set e, the posterior probability of the parameter p is expressed by the multiplication of the likelihood and the prior probability of the parameter,

$$P'(p|e) \propto L(p|e) \times P(p), \tag{24}$$

where $P'(p|e)$ is the posterior probability, $L(p|e)$ is the likelihood, and $P(p)$ is the prior probability of the parameter. If we assume that the distribution of the observation data follows the Gaussian distribution, the likelihood from these measurements is given by

$$L(p|e) = \prod_{i,j} \frac{1}{\sqrt{2\pi\sigma_{i,j}^2}} \exp\left[-\frac{\left(e_{i,j}^{\mathrm{data}} - e_i(p)\right)^2}{2\sigma_{i,j}^2}\right], \tag{25}$$

where $e_{i,j}^{\mathrm{data}}$ and $\sigma_{i,j}^2$ are the measured value and the variance of the observation data of the stacked void of the radius $R_{\mathrm{eff},j}$ at z_i and $e_i(p)$ is the theoretical predicted value for the component with the parameter p at z_i. In this demonstration of the AP test, z_i means one of the redshift bins while $R_{\mathrm{eff},j}$ means one of the radii of the stacked void, where $R_{\mathrm{eff}} = 5, 6, \cdots, 15\,\mathrm{Mpc}\,h^{-1}$. p includes a set of Ω_{m} and w. Hence the theoretical prediction $e_i(p)$ is evaluated as

$$e_i(\Omega_{\mathrm{m}}, w) \equiv \left.\frac{\Delta z}{z\Delta\theta}\right|_{\mathrm{theory},i} = \frac{1}{cz_i}\chi(z_i, \Omega_{\mathrm{m}}, w)H(z_i, \Omega_{\mathrm{m}}, w). \tag{26}$$

On the other hand, e_i^{data} is obtained through

$$e_{i,j}^{\mathrm{data}} \equiv \left.\frac{\Delta z}{z\Delta\theta}\right|_{\mathrm{data},i,j} = \frac{1}{cz_i}\chi(z_i)H(z_i)\sqrt{\frac{\Delta x_\parallel^2(z_i, R_{\mathrm{eff},j})}{\Delta x_\perp^2(z_i, R_{\mathrm{eff},j})}}, \tag{27}$$

where we use the mean value in Fig. 4 as $\Delta x_\parallel^2/\Delta x_\perp^2$ and the fiducial values of matter density and equation-of-state parameter, $\Omega_{\mathrm{m,\,fid}} = 0.3089$ and $w_{\mathrm{fid}} = -1$, which are adopted in the IllustrisTNG300-3. For the Markov-Chain Monte-Carlo (MCMC) analysis, we use a python module EMCEE (Foreman-Mackey et al. 2013).

We plot the probability distribution of the parameters obtained by the MCMC analysis in Fig. 5. The results show that the parameter estimation is consistent with the fiducial values within a 1σ confidence level. The estimated values with 1σ errors are $\Omega_{\mathrm{m}} = 0.3031^{+0.0067}_{-0.0066}$ and $w = -1.010^{+0.043}_{-0.044}$. Especially, the estimation of w is very close to the fiducial value while that of Ω_{m} is barely consistent with the 1σ region. The estimation of matter density has uncertainty about 2 per cent. This result is derived by only the AP signals of the stacked void. The current joint analysis of the CMB power spectrum, CMB lensing, and Baryon Acoustic Oscillation (BAO) reported the uncertainty on Ω_{m} is about 2 per cent (Planck Collaboration VI 2020) when they assume the ΛCDM model. Our analysis result achieves almost the same level estimation as the current detailed cosmological
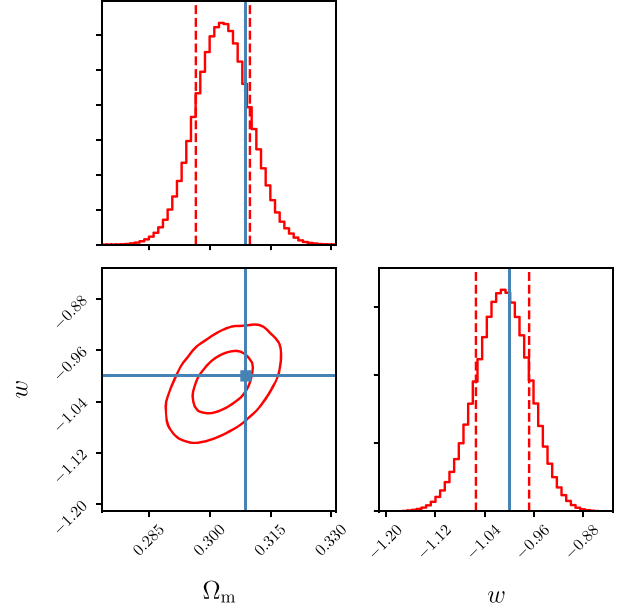

Figure 5. Expected parameter constraints given our simulation volume in the real space. The expected error is obtained by stacking all voids found in the simulation volume. For 2D contour, the circles correspond to 1σ and 2σ confidence regions and 1D histogram is a likelihood marginalized over other parameters. The best-fitting value for each parameter is $\Omega_{\mathrm{m}} = 0.3031^{+0.0067}_{-0.0066}$ and $w = -1.010^{+0.043}_{-0.044}$. Our fiducial value is indicated by the blue dot. As we see in Fig. 4, the stacked void is well described by the sphere so that the AP test correctly measures the cosmological parameters.

observation. Therefore, the AP test with stacked voids in the 21 cm intensity maps has the potential to provide stronger constraints on the cosmological parameters rather than AP test with stacked voids in galaxy distributions.

Before ending this section, we comment on the observation noise. In this work, we do not consider any contamination such as foreground effects or equipment noises, and the angular and frequency resolution of radio telescopes. In our method, we use the contour line corresponds to the threshold to trace the shape of the voids. Although we set the threshold to the mean value in the map, we can freely choose this threshold. To identify the shapes of the structures in actual observations, it is required that the threshold is larger than the noise level. In lower redshifts, $z < 5$, the dominant noise contribution comes from the thermal noise of observation equipment. We confirm that the noise level might be higher than the means signals in this observation set up at $1 < z$ when we assume the instrumental noise (Horii et al. 2017). In this case, we can set the threshold to the higher value so that we can trace the void structures.

4 THE RSD EFFECT

The peculiar velocity of the H$_{\mathrm{I}}$ gas gives two effects on the 21 cm signals. One is the broadening of the line spectrum, which contributes through $V_\parallel$ in equation (3). As mentioned above, this effect is subdominant compared with the Hubble velocity. Therefore, we neglect it in this paper.

The other effect is the RSD. The observed positions of the intensity signals are modified along the line-of-sight direction because the redshift is affected by Hubble expansion as well as Doppler shift due to the peculiar velocity, which cannot be discriminated. In this
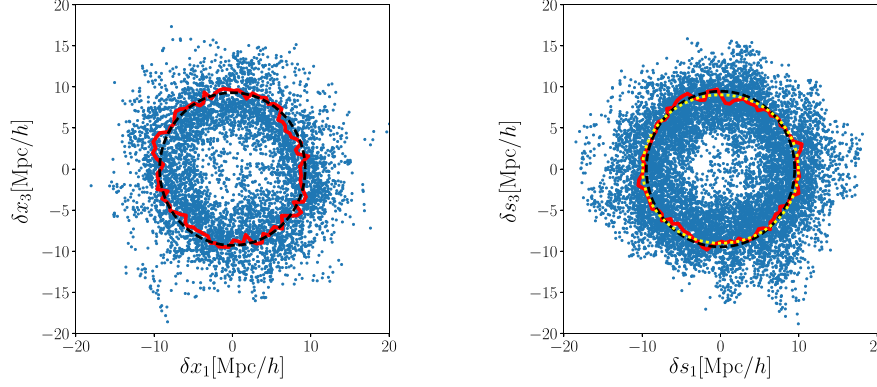
Figure 6. The comparison of stacked void shape in real space and redshift space. The left-hand panel is the shape of the voids in real space and the right-hand panel shows the one in redshift space, after stacking over 100 voids which have $R_{\rm eff} = 10 \pm 0.5$ [Mpc h^{-1}] at $z = 1$. The yellow dotted line indicates the ellipsoid which is fitted to the red line, where the best-fitting ratio between the major and minor axes being 0.9075.

section, we discuss the RSD effect on the void findings and the AP test in the 21 cm intensity maps.

To take into account the RSD effect, we construct the intensity maps in redshift space. The procedures are the same as in the real space but first of all, we shift the position of gas particles according to their peculiar velocities along the line-of-sight direction,

$$s_{\|} = x_{\|} + \frac{(1+z)v_{\rm p\|}}{H(z)}. \tag{28}$$

Then gridding, converting to the brightness temperature, particle re-distribution and void finding procedures are all same as in the real space.

4.1 Void shape in redshift space

In redshift space, we have confirmed that the stacked voids become squashed along the line of sight, which is also found in the previous studies in dark matter density fields or mock galaxy distributions (Lavaux & Wandelt 2012; Mao et al. 2017). Fig. 6 demonstrates how the stacked void shape is deformed in the redshift space (right) compared to the one in the real space (left). For both panels, we set vertical axes as the line-of-sight. The yellow dotted curve in the right-hand panel shows the best-fitting ellipse to the measured profile shown by the red solid line. Compared to the perfect circle shown by the black dashed line, the ellipse is squashed along the line-of-sight direction.

To show the impact of the RSD effect on the shape deformation, we plot the ratio, $\Delta s_{\|}/\Delta s_{\perp}$, in Fig. 7. The RSD effect appears by about 10 per cent level flattening of stacked voids along the line-of-sight direction. It does not depend on the void size but does on the redshift. The 10 per cent distortion due to the RSD has been already found in the previous works with N-body simulations, where dark matter particles or mock galaxies are used as a tracer of the void (Lavaux & Wandelt 2012; Mao et al. 2017). The previous works reported that the shape distortion is about 10–15 per cent at $z < 1$, which is consistent with our results.

4.2 AP test in redshift space

Here we present the cosmological parameter estimation using the AP test in the presence of the RSD effect. If we do not consider the RSD effect in redshift space, $\Omega_{\rm m}$ and w are both underestimated, since
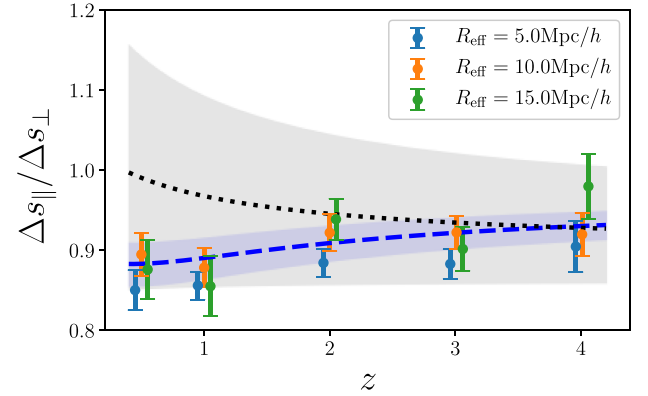

Figure 7. The same as Fig. 4, but in redshift space. The redshift-space distortion effect does not depend on the void size but redshift. The blue dashed line is the best-fitting curve of equation (31) with keeping cosmological parameters to their input values. The black dotted line is the one with all parameters including $\Omega_{\rm m}$ and w are simultaneously fitted.

smaller values of $\Omega_{\rm m}$ and w make AP signal (equation (19)) smaller. Previous works attempt to correct the RSD effect by multiplying a constant factor (Lavaux & Wandelt 2012; Sutter et al. 2014b; Mao et al. 2017) and make the parameter estimation unbiased. However, as can be seen in Fig. 7, the offset from unity is not constant in our case simply because we consider a wide range of redshift at the same time. We find that the factor of $0.9071^{+0.0032}_{-0.0031}$ is reasonable to describe the offset so that we need to divide the AP signals by this factor to correct for the RSD effect with the constant offset. With this correction, the estimated cosmological parameters are highly biased, which reflects the model of correcting the RSD effect by the constant factor is not appropriate.

In our analysis, we assume that the deformation depends on the redshift due to the velocity evolution. Here, similarly to Hamaus et al. (2015, 2016), we model the time dependence based on the linear perturbation theory. We can expand $\Delta s_{\|}/\Delta s_{\perp}$ as

$$\frac{\Delta s_{\|}^2}{\Delta s_{\perp}^2} = \frac{1}{\Delta x_{\perp}^2} \left[\langle \delta x_{\|}^2 \rangle + 2 \frac{(1+z)\langle \delta x_{\|} \cdot v_{\rm p\|} \rangle}{H(z)} + \frac{(1+z)^2 \langle v_{\rm p\|}^2 \rangle}{H(z)^2} \right]. \tag{29}$$
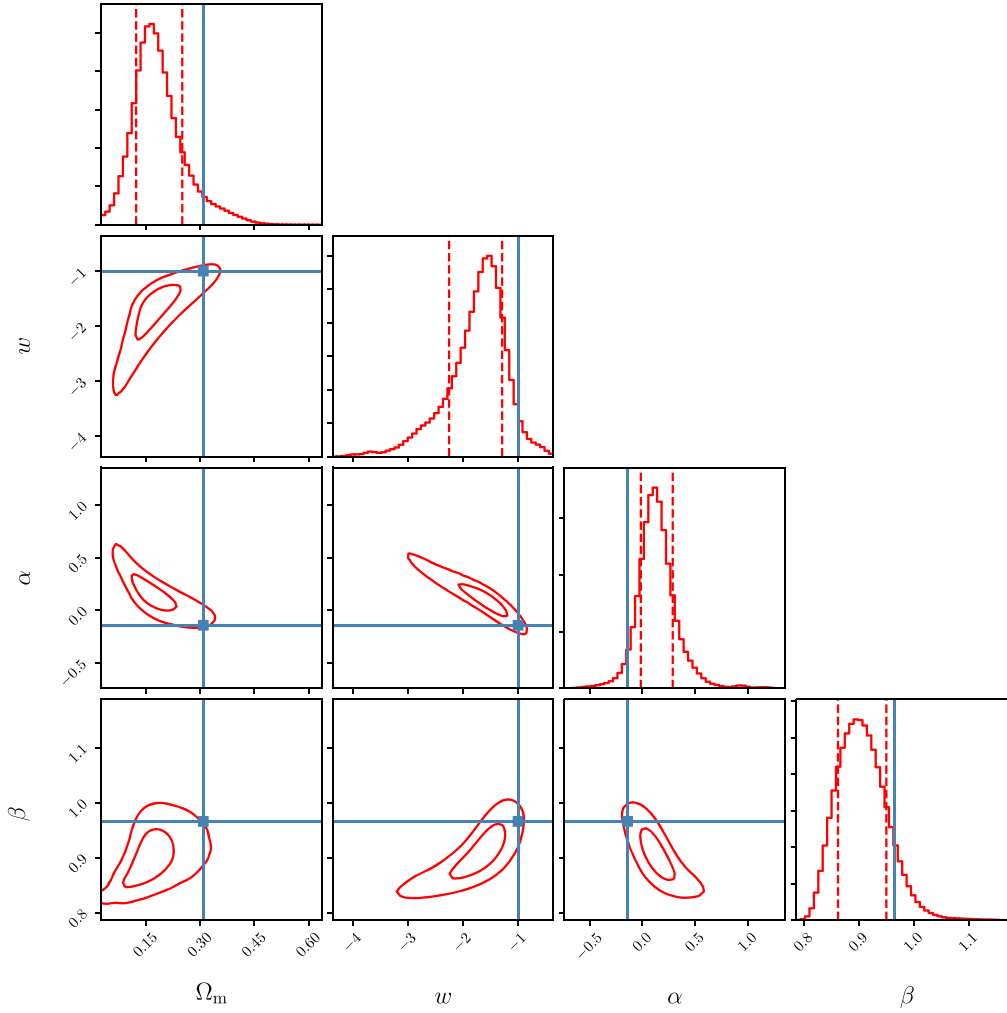
Figure 8. Same as Fig. 9 but all the parameters are jointly fitted simultaneously. We find that the RSD correction parameters and cosmological parameters are largely degenerate with each other. The estimated value for the cosmological parameters are biased; however, it is still consistent within 2σ. The best-fitting values are $\Omega_{\rm m} = 0.1723^{+0.0734}_{-0.0560}$, $w = -1.692^{+0.385}_{-0.663}$, $\alpha = 0.1329^{+0.1830}_{-0.1409}$, and $\beta = 0.9016^{+0.0480}_{-0.0427}$.

According to the linear theory, the peculiar velocity is related to the density perturbation at $z = 0$,

$$\boldsymbol{v}_{\rm p}(\boldsymbol{x}) = \frac{H(z)f(z)D(z)}{(1+z)} \int {\rm d}^3 x' \frac{\boldsymbol{x} - \boldsymbol{x}'}{|\boldsymbol{x} - \boldsymbol{x}'|^3} \delta(\boldsymbol{x}', z=0), \qquad (30)$$

where $f(z)$ and $D(z)$ are the linear growth rate and the linear growth factor, respectively. From equations (29) and (30), we can approximate

$$\frac{\Delta s_\parallel}{\Delta s_\perp} \simeq \sqrt{\frac{\langle \delta x_\parallel^2 \rangle}{\Delta x_\perp^2}} + \frac{(1+z)\langle v_{p\parallel} \rangle}{H(z)\sqrt{\Delta x_\perp^2}} = \beta + \alpha f(z)D(z), \qquad (31)$$

where in the second equality, we isolate the redshift-dependent term and replace the rest of the term with parameter α instead of estimating the density profile in equation (30). We further introduce the parameter β to absorb possible systematic uncertainties which may arise due to the imperfect spherical shape of voids in real space. We use this time dependence model, equation (31), to correct the RSD effect instead of the constant offset applied in Lavaux & Wandelt (2012), Sutter et al. (2014b), Mao et al. (2017). In the case where the perturbation is well within the linear regime and in the absence

of velocity biases, the parameters α and β can be predictable from the linear theory. However, in practice, the values predicted by the linear theory do not explain the amount of deformation by the RSD and we leave them as free parameters.

First, we fit the AP signal with cosmological parameters and calibration parameters in equation (31) simultaneously. In Fig. 8, we show the constraints on those parameters. The blue solid lines represent the fiducial values. The fiducial values for nuisance parameters α and β can be defined later in this section. One can see that the estimations deviate from the fiducial values when we search the preferable parameters at the same time, in more than 1σ but less than 2σ. In this case, $\Omega_{\rm m}$ and w are under estimated by the parameter search such that $\Omega_{\rm m} = 0.1723^{+0.0734}_{-0.0560}$ and $w = -1.692^{+0.385}_{-0.663}$. The reason for these wrong estimations comes from the incorrect estimations of the correction parameters, α and β. According to the results, we obtain $\alpha = 0.1329^{+0.1830}_{-0.1409}$ and $\beta = 0.9016^{+0.0480}_{-0.0427}$. In Fig. 7, we plot the offset function as the black dotted line. One can see that the offset function does not well trace the data, particularly at low redshifts. Therefore, the estimated cosmological parameters are biased. As shown in Fig. 8, the nuisance parameters degenerate
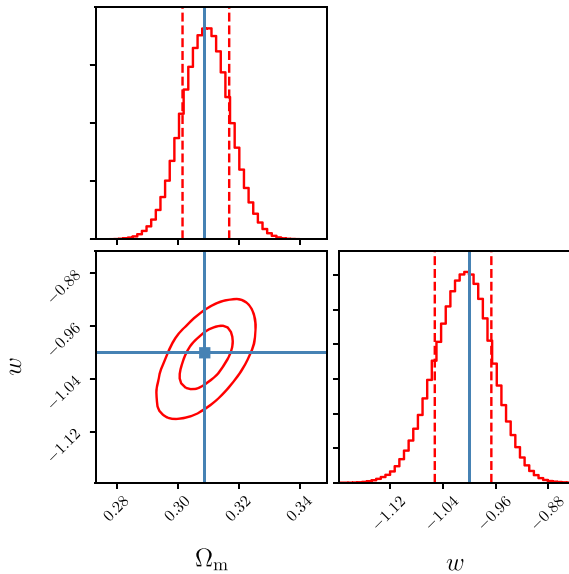
Figure 9. Expected errors at redshift space. We correct for the redshift-space distortion by equation (31). The values for α and β are obtained by assuming $\Omega_{\rm m}$ and w being at their fiducial values. After the correction, we estimate the cosmological parameters and find their best-fitting values as $\Omega_{\rm m} = 0.3093^{+0.0076}_{-0.0077}$ and $w = -1.008^{+0.042}_{-0.044}$.

with the cosmological parameters, which indicates that the tight and correct constraints on the calibration are required to make the estimate accurate and precise.

Then, we would like to see whether this calibration model may work when the parameters are properly provided a priori. To do this, we fix the cosmological parameters to their fiducial values and find the best-fitting values for α and β, which results in $\alpha = -0.1424^{-0.0271}_{-0.0272}$ and $\beta = 0.9660^{+0.0118}_{-0.1160}$. We refer to these values for α and β as fiducial values aforementioned. The predicted distortion is shown in Fig. 7 with blue dashed line. The prediction nicely recovers the observed distortion at all redshift ranges. Given the fiducial values for α and β, we run the likelihood analysis only for the cosmological parameters.

Then we have the best-fitting parameters as $\Omega_{\rm m} = 0.3093^{+0.0076}_{-0.0077}$ and $w = -1.008^{+0.042}_{-0.044}$, which are fairly consistent with the fiducial values by the same uncertainty level as in the case without the RSD effect. Therefore, as long as we can calibrate the RSD effect via simulation as prior knowledge, the model well describes the RSD correction and we can measure the cosmological parameters in an unbiased manner.

5 CONCLUSION

In this paper, we have presented the AP test with the 21 cm voids as a new cosmological parameter estimation in future 21 cm observations. To demonstrate the AP test, we have constructed the 21 cm intensity maps by using the state-of-the-art cosmological hydrodynamics simulation, the IllustrisTNG300-3. Then, using the void finder algorithm VIDE, we made void catalogues in which the void shapes are identified through tracing the critical intensity contour. The shape of the individual void is far from spherical. However, we have shown that the stacked void becomes more spherical as increasing the number of voids to be stacked. This result suggests that the voids in the 21 cm intensity maps are appropriate for the AP test.

To present the potential ability of the AP test with the stacked void of the 21 cm intensity maps, we have performed the Markov Chain Monte Carlo analysis for the parameter estimation on the matter-energy density parameter and the equation of state of dark energy. Our result shows that the parameter estimation by the AP test with 21 cm stacked voids is consistent with the fiducial values within 1σ confidence level. In particular, in the estimation of the matter-energy density parameter, the uncertainty level can be controlled in about 2 per cent, which is the same level as the result of the joint analysis among CMB temperature anisotropy, CMB lensing, and BAO.

Similar to the case with voids in galaxy maps, the RSD effect is one of the challenges in the AP test with 21 cm intensity maps. The peculiar velocities of neutral hydrogen gas deform the void shapes in 21 cm intensity maps. To investigate the impact of the RSD effect on the AP test, we construct the redshift-space 21 cm intensity maps with the RSD effect. We found that the RSD effect arises as the flattening effect on the void shape along the line-of-sight direction by about 10 per cent level, compared to the intensity map without the RSD effect. To remove the RSD effect in the AP test, we have suggested the correction factor whose redshift evolution is motivated from the one of the peculiar velocity in the linear perturbation theory. We have shown that we can correct the RSD effect and recover the same uncertainty level as in the case without the RSD effect when we successfully calibrate the correction factor. Thus, our results strongly encourage to apply stacked voids in the $H_{\rm I}$ intensity maps to the AP test. We will conduct further investigation of how we calibrate the correction factor by performing the numerical simulations with different cosmological models.

DATA AVAILABILITY

The data underlying this article are available in IllustrisTNG simulation, at https://www.tng-project.org/.

REFERENCES

Abazajian K. N. et al., 2009, ApJS, 182, 543
Ahn C. P. et al., 2014, ApJS, 211, 17
Alam S. et al., 2015, ApJS, 219, 12
Alcock C., Paczynski B., 1979, Nature, 281, 358
Allison A. C., Dalgarno A., 1969, ApJ, 158, 423
Ballinger W. E., Peacock J. A., Heavens A. F., 1996, MNRAS, 282, 877
Clampitt J., Cai Y.-C., Li B., 2013, MNRAS, 431, 749
Correa C. M., Paz D. J., Padilla N. D., Ruiz A. N., Angulo R. E., Sánchez A. G., 2019, MNRAS, 485, 5761
Eisenstein D. J. et al., 2005, ApJ, 633, 560
Endo T., Nishizawa A. J., Ichiki K., 2018, MNRAS, 478, 5230
Field G. B., 1958, Proc. IRE, 46, 240
Field G. B., 1959, ApJ, 129, 536
Foreman-Mackey D., Hogg D. W., Lang D., Goodman J., 2013, PASP, 125, 306
Furlanetto S. R., Oh S. P., Briggs F. H., 2006, Phys. Rep., 433, 181
Glazebrook K., Blake C., 2005, ApJ, 631, 1
Haardt F., Madau P., 2012, ApJ, 746, 125

Hamaus N., Sutter P. M., Lavaux G., Wand elt B. D., 2015, J. Cosmol. Astropart. Phys., 2015, 036

Hamaus N., Pisani A., Sutter P. M., Lavaux G., Escoffier S., Wand elt B. D., Weller J., 2016, Phys. Rev. Lett., 117, 091302

Horii T., Asaba S., Hasegawa K., Tashiro H., 2017, PASJ, 69, 73

Hu W., Haiman Z., 2003, Phys. Rev. D, 68, 063004

Hu W., Sugiyama N., 1996, ApJ, 471, 542

Komatsu E. et al., 2011, ApJS, 192, 18

Kuhlen M., Madau P., Montgomery R., 2006, ApJ, 637, L1

Lavaux G., Wandelt B. D., 2012, ApJ, 754, 109

Liszt H., 2001, A&A, 371, 698

Mao Q., Berlind A. A., Scherrer R. J., Neyrinck M. C., Scoccimarro R., Tinker J. L., McBride C. K., Schneider D. P., 2017, ApJ, 835, 160

Marinacci F. et al., 2018, MNRAS, 480, 5113

Matsubara T., 2004, ApJ, 615, 573

Matsubara T., Suto Y., 1996, ApJ, 470, L1

Naiman J. P. et al., 2018, MNRAS, 477, 1206

Nelson D. et al., 2018, MNRAS, 475, 624

Nelson D. et al., 2019, Comput. Astrophys. Cosmol., 6, 2

Neyrinck M. C., 2008, MNRAS, 386, 2101

Park D., Lee J., 2007, Phys. Rev. Lett., 98, 081301

Perlmutter S. et al., 1999, ApJ, 517, 565

Pillepich A. et al., 2018, MNRAS, 475, 648

Pisani A., Sutter P. M., Hamaus N., Alizadeh E., Biswas R., Wandelt B. D., Hirata C. M., 2015, Phys. Rev. D, 92, 083531

Planck Collaboration XIII, 2016, A&A, 594, A13

Planck Collaboration VI, 2020, A&A, 641, A6

Platen E., van de Weygaert R., Jones B. J. T., 2007, MNRAS, 380, 551

Platen E., van de Weygaert R., Jones B. J. T., 2008, MNRAS, 387, 128

Riess A. G. et al., 1998, AJ, 116, 1009

Ryden B. S., 1995, ApJ, 452, 25

Santos M. et al., 2015, Proc. Sci., Cosmology from a SKA HI Intensity Mapping Survey. SISSA, Trieste, PoS(AASKA14)019

Seo H.-J., Eisenstein D. J., 2003, ApJ, 598, 720

Shandarin S., Feldman H. A., Heitmann K., Habib S., 2006, MNRAS, 367, 1629

Shandarin S. F., Sheth J. V., Sahni V., 2004, MNRAS, 353, 162

Smith F. J., 1966, Planet. Space Sci., 14, 929

Springel V., 2010, MNRAS, 401, 791

Springel V. et al., 2018, MNRAS, 475, 676

Square Kilometre Array Cosmology Science Working Group et al., 2020, Publ. Astron. Soc. Aust., 37, e007

Sutter P. M., Lavaux G., Wandelt B. D., Weinberg D. H., 2012a, ApJ, 761, 187

Sutter P. M., Lavaux G., Wandelt B. D., Weinberg D. H., 2012b, ApJ, 761, 44

Sutter P. M., Lavaux G., Wandelt B. D., Weinberg D. H., Warren M. S., Pisani A., 2014a, MNRAS, 442, 3127

Sutter P. M., Pisani A., Wandelt B. D., Weinberg D. H., 2014b, MNRAS, 443, 2983

Sutter P. M. et al., 2015, Astron. Comput., 9, 1

van de Weygaert R., van Kampen E., 1993, MNRAS, 263, 481

Verza G., Pisani A., Carbone C., Hamaus N., Guzzo L., 2019, J. Cosmol. Astropart. Phys., 12, 040

Weinberg D. H., Mortonson M. J., Eisenstein D. J., Hirata C., Riess A. G., Rozo E., 2013, Phys. Rep., 530, 87

Wouthuysen S. A., 1952, AJ, 57, 31

Xu G., 1995, ApJS, 98, 355

Zivick P., Sutter P. M., 2016, in van de Weygaert R., Shandarin S., Saar E., Einasto J., eds, IAU Symp. Vol. 308, The Zeldovich Universe: Genesis and Growth of the Cosmic Web. Cambridge Univ. Press, Cambridge, p. 589

Zygelman B., 2005, ApJ, 622, 1356

This paper has been typeset from a TeX/LaTeX file prepared by the author.